Acta Materialia 145 (2018) 19–29

Contents lists available at ScienceDirect

Acta Materialia

journal homepage: www.elsevier.com/locate/actamat

Full length article

Sample-size-dependent surface dislocation nucleation in nanoscale crystals

Qing-Jie Li [a], Bin Xu [b], Shotaro Hara [c, *], Ju Li [d, e, **], Evan Ma [a, ***]

[a] Department of Materials Science and Engineering, Johns Hopkins University, Baltimore, MD 21218, USA
[b] School of Materials Science and Engineering, Shanghai Jiao Tong University, 800 Dongchuan Road, Minhang, Shanghai 200240, China
[c] Department of Mechanical Engineering, Faculty of Engineering, Chiba Institute of Technology, 2-17-1 Tsudanuma, Narashino, Chiba 275-0016, Japan
[d] Department of Nuclear Science and Engineering, Massachusetts Institute of Technology, Cambridge, MA 02139, USA
[e] Department of Materials Science and Engineering, Massachusetts Institute of Technology, Cambridge, MA 02139, USA

ARTICLE INFO

Article history:
Received 8 August 2017
Received in revised form
17 November 2017
Accepted 20 November 2017
Available online 1 December 2017

Keywords:
Nanoscale crystals
Surface dislocation nucleation
Surface stresses
Sample size effects

ABSTRACT

The finite-temperature mechanical strength of nanoscale pristine metals at laboratory strain rates may be controlled by surface dislocation nucleation, which was hypothesized to be only weakly dependent on the sample size. Previous studies on surface dislocation nucleation investigated factors such as surface steps, oxidation layers and surface diffusion, while the role of surface stresses and sample size remains unclear. Here we perform systematic atomistic calculations on the activation free energy barriers of surface dislocation nucleation in sub-50 nm nanowires. The results demonstrate that surface stresses significantly influence the activation processes of surface dislocation nucleation. This renders the strength strongly dependent on sample size; whether it is "smaller is stronger" or "smaller is weaker" depends on the combined effects of surface stress and applied axial stress, which can be universally explained in terms of the local maximum resolved shear stress. A linear relation between the activation entropy and activation enthalpy (Meyer-Neldel compensation rule) was found to work well across a range of stresses and sample sizes.

1. Introduction

Nanomanufacturing can create small-volume (with length scale of 10^1–10^2 nm) metals that contain little or no defects [1–7]. These *nanoscale pristine* metals represent an extreme state of crystals: they are free of pre-existing dislocations but have very high surface-to-volume ratio. (Indeed, one reason for the lack of dislocation storage is that image attractions to free surfaces tend to destabilize dislocation networks.) At low homologous temperatures, when nanoscale pristine metals are subjected to relatively high external stress, it is widely believed that plastic deformation initiates via thermally activated nucleation of dislocations on the surfaces [7–15]. This surface dislocation nucleation (SDN) process has been shown to be highly sensitive to surface conditions [16]. For example, the local configurations of surfaces such as surface steps [17–19], local morphology [13] and oxidation layers [20] can significantly influence the activation parameters of SDN. Mass-action processes such as surface diffusion of atoms may also couple strongly with SDN [7]. In addition to these extrinsic surface conditions and processes, large surface stresses are ubiquitous in nanoscale pristine metals as a result of the under-coordinated surface atoms [21–25]. These surface stresses are believed to impose intrinsic limits on the mechanical strength of nanoscale pristine metals [9,13,26–28], but their effects have not been investigated in detail.

SDN has been studied before from different perspectives. For example, within the framework of continuum mechanics, the activation energy of SDN has been usually modeled by analyzing individual contributions such as the elastic energy, stacking fault energy, surface ledge energy, etc [9,10,29,30]. These models generally suffer from the uncertainties on the dislocation core cutoff parameters employed. Alternatively, SDN has been treated based on the Peierls-Nabarro dislocation model [31], which incorporates atomistic information into the continuum approach. Computationally, activation parameters of SDN have been

---

[*] Corresponding author.
[**] Corresponding author. Department of Nuclear Science and Engineering, Massachusetts Institute of Technology, Cambridge, MA 02139, USA.
[***] Corresponding author.
E-mail addresses: hara.shotaro@p.chibakoudai.jp (S. Hara), liju@mit.edu (J. Li), ema@jhu.edu (E. Ma).

https://doi.org/10.1016/j.actamat.2017.11.048
1359-6454/

calculated using either reaction pathway sampling methods [8,9] or hyperdynamics simulations [32]. Generally, activation parameters obtained either analytically or computationally are stress dependent, which are then fed into finite-temperature transition-state theories whereby the nucleation stress can be obtained numerically for different strain rates. Such a modeling framework combining atomistic simulations/continuum mechanics and reaction rate theories has been shown to be useful in predicting the mechanical strength over a range of temperatures and strain rates that can be directly compared with laboratory experiments.

While the mechanical strength of nanoscale pristine metals has been successfully modeled with respect to external variables such as temperature and strain rate, the intrinsic sample size effects have only been treated briefly [8–10,30]. For example, surface effects were modeled by adding image forces to the nucleated dislocation loop, leading to an extra contribution to the activation free energy [10,30]. Also, surface stresses were taken into account by removing the surface-induced axial stress from the total axial stress during calculations [9]. In addition, it was shown that the number of SDN sites decreasing with sample size brings in a strengthening effect [8]. However, these studies focus mostly on the overall trend of material strength with respect to sample size. The exact role played by surface stresses in SDN remains unresolved.

Currently, there are several difficulties in understanding the intrinsic surface stress effects on SDN for both continuum modeling and atomistic calculations. First, the continuum mechanics framework requires numerical parameters from atomistic simulations. Second, how surface stresses contribute to the axial stress dependence and sample size dependence of the activation parameters is unclear. Third, the surface stresses effects may depend on many factors such as the geometry of the nanoscale sample, surface energy, crystallography and externally applied stress level, etc.; the most important factors need to be identified. Last but not least, current reaction pathway sampling methods such as free-end nudged elastic band (NEB) [8,33] or string method [9,34] are computationally too expensive to calculate the activation parameters for experimentally relevant samples (e.g., tens of nanometers in diameter, for a nanowire). Consequently, most previous studies only focused on very small sample sizes [8,9] (a few nanometers for the diameter of a nanowire) and the activation parameters obtained cannot be directly applied to larger samples.

In this work, we employ a modified activation-relaxation technique *nouveau* (ARTn) [35–37] to obtain the zero-T activation Gibbs free energy ($\Delta G_0(\sigma)$) or activation enthalpy ($\Delta H(\sigma) \equiv \Delta G_0(\sigma)$) for nanowires with diameters up to 50 nm, an experimentally relevant length scale that has been computationally prohibitive for typical transition path sampling techniques such as free-end nudged elastic band method [8,33] or free-end string method [34]. Based on the calculation results, the intrinsic surface stress effects on activation enthalpy have been evaluated. Furthermore, by using constrained molecular dynamics and thermodynamic integration method, we compute the *finite-temperature* activation Gibbs free energies $\Delta G(\sigma,T)$ that include thermal uncertainties (entropy) in the transition paths. By comparing the numerical $\Delta H(\sigma)$ and $\Delta G(\sigma,T)$, we discover the Meyer-Neldel (M-N) compensation rule [38] largely works in the parameter range relevant to laboratory timescale (strain-rate) experiments. A single parameter T_{MN}, on the order of 900 K, can thus describe finite-temperature $\Delta G(\sigma,T)$, if the zero-temperature $\Delta H(\sigma)$ is known. Based on the calculated $\Delta H(\sigma)$ for SDN, we found obvious sample size dependence of strength for the sub-50 nm nanoscale pristine metals; the generally believed "smaller is stronger" trend is only valid when the external load counteracts the Laplace pressure [21] due to surface stresses, and it becomes "smaller is weaker" when the external load constructively superimposes on the Laplace pressure.

2. Simulation methods

We choose Cu nanowire with characteristic size from 2 nm to 50 nm as our model samples. Specifically, two widely studied types [8,9] of nanowires are considered in the current work, i.e., [100] oriented square nanowire under compressive loading and [110] oriented rhombic nanowire under tensile loading. Empirical potential for Cu [39] is used to describe the interatomic interactions. All nanowires have periodic boundary conditions in the axial direction and free surfaces in other directions. The aspect ratio for all nanowires is 2.5. First, different sized nanowires are elastically strained to the athermal stress limit using the athermal quasi-static loading method. During athermal quasi-static loading, energy minimization after each strain increment is performed via the conjugate gradient method. The strain increment is 0.05% while the force tolerance for energy minimization is 0.001 eV/Å. Then, the configurations of nanowires at different stress levels are extracted to first calculate the zero-T activation barrier.

In order to efficiently calculate the zero-T activation Gibbs free energies $\Delta G_0(\sigma) \equiv \Delta H(\sigma)$ for samples with sizes up to 50 nm, we employ ARTn [35–37] but with modifications based on the known information about the minimum energy path (MEP). The pathways searched by ARTn highly depend on the initial searching direction on the potential energy landscape (PEL), and choosing an appropriate initial direction could efficiently accelerate ARTn. The initial search direction can be specified in two ways. One way is to take advantage of athermal quasi-static loading, i.e., with increasing strain, the sample will finally reach a saddle point of the SDN event. Though saddle points differ from each other under different strains, they generally locate in a similar direction on the PEL with respect to the initial configurations. Thus, we can choose our initial searching direction as the displacement vector (plus a random noise vector) between the configuration at current strain and the configuration at the elastic limit during athermal quasi-static loading. For events that cannot be observed during athermal quasi-static loading but with known information on their MEP, a second way is to 'manually' manipulate atoms of interest to construct a tentative configuration near the saddle points of the potential MEP. Then the displacement vector (plus a random noise vector) between this tentative configuration and the initial configuration can be used as the search direction in ARTn. After choosing an appropriate initial search direction, the system is pushed step by step (at each step energy minimization is performed in the perpendicular hyperplane) along this direction and is considered to be out of the potential well when the smallest eigenvalue of the Hessian matrix falls below a negative threshold. Then, the search direction is switched to the eigenvector direction associated with the smallest eigenvalue of the Hessian matrix. The system is slightly activated along the eigenvector direction and energy minimization is performed in the perpendicular hyperplane after each activation. The eigenvector associated with the smallest eigenvalue of the Hessian matrix is updated before each activation, using the Lanczos algorithm. The system is considered to reach a first-order saddle point when the smallest eigenvalue of the Hessian matrix is negative and the magnitude of the hyper-space force vector is below 0.001 eV/Å. In this way, the modified ARTn algorithm can efficiently converge to the saddle point of SDN at different stresses.

Compared to the free-end NEB method, our modified ARTn can significantly reduce the computational cost in finding the saddle point. The factors contributing to this include a) only one configuration is used in ARTn while many replicas have to be used in NEB method to construct the 'elastic band' and b) NEB method updates individual replicas by also considering the inter-replica interactions whereas ARTn updates the single configuration solely based on interatomic interactions within the configuration, significantly increasing the efficiency of finding saddle points for large samples. Note however that the modified ARTn requires known information on the transition pathway to accelerate the saddle-finding process; in cases where the actual transition paths are entirely unknown, the modified ARTn should be applied with caution to avoid missing important events.

Activation free energies at finite temperature are evaluated using thermodynamic integration method. First, the MEP was found using free-end [8,33] and climbing image [40] NEB method. Then based on the local tangent direction $\boldsymbol{\tau}_{\mathrm{i}}$ for each replica, we perform molecular dynamics for all replicas with a constraint of $(\boldsymbol{v}\cdot\boldsymbol{\tau}) = 0$, where $\boldsymbol{v}$ is the hyperspace velocity vector for each replica. The constraint $(\boldsymbol{v}\cdot\boldsymbol{\tau}) = 0$ means that the hyper-space velocity vector along the local tangent direction of the 'elastic band' is kept zero. Thus, all replicas are constrained to relax in the perpendicular hyperplanes. In this way, the relaxation along the local tangent direction is excluded and the unstable intermediate replicas can thus maintain their relative spacing along the 'elastic band'. For practical implementation, the local tangent direction is kept the same as the initial one. We can view such dynamics as the fluctuations of the whole MEP under thermal energy. Therefore, all replicas may not be exactly constrained into the initial path and their time-averaged positions may be slightly shifted from the initial NEB path position. All replicas are considered to be well relaxed when the time-averaged perpendicular force component $F_i^{\perp}$ is less than 5×10^{-5} eV/Å. Finally, we carried out thermodynamic integration for the well relaxed path to get activation Gibbs free energy $\Delta G = \int \left| -F^{\parallel} \right| d\lambda$, where λ is the hyper space arc length. It should be noted that sufficient number of replicas on the integration path should be used to fully represent the actual MEP. In the present work, all replicas are relaxed at 300 K and 48 and 96 images are used for 5 nm and 10 nm nanowire, respectively. Our simulations are performed mainly based on the LAMMPS package [41] and visualized using the AtomEye package [42].

3. Results and discussions

3.1. Surface-stress-induced internal stresses

In nanoscale single crystals, a significant fraction of the constituent atoms resides on free surfaces. These under-coordinated surface atoms have different chemical bonding environment from the interior atoms, thus resulting in different equilibrium interatomic spacing compared to the interior atoms. As a result, the interior atoms equivalently exert a stress onto the surface atoms (the so-called surface stress) or *vice versa* (Laplace pressure) [21]. Thus, even for well relaxed free-standing nanoscale single crystals, non-zero internal stresses exist. For example, a fully relaxed free-standing nanowire is usually subjected to an average internal axial stress

$$\sigma_0 = g\frac{f}{D} \tag{1}$$

where f is surface stress defined as $f_{ij} = \gamma\delta_{ij} + \partial\gamma/\partial\varepsilon_{ij}$ (γ is surface energy, δ_{ij} is the Kronecker delta function and ε_{ij} is the applied strain), D is the characteristic length of the nanowire (e.g., the diameter) and g is a geometrical factor. Note that f_{ij} is a second rank tensor which can be reduced to the diagonal components when principal axes are used (off-diagonal components are zero). These diagonal components can be further reduced to a single variable f if the surface has higher symmetry. In the current work, {100} and {111} surfaces of face-center-cubic structure are used, so we will denote the surface stresses simply as f. Detailed derivation of Equation (1) can be found in *Supplementary Materials*. Fig. 1 shows the average internal axial stress σ_0 of different sized nanowires and the corresponding atomic stress tensor component $S^i_{\alpha\alpha}$(α means the axial direction and i is the atom index) for each atom (the insets). In our simulation, the average internal axial stress is obtained by $\sigma_0 = 1/N_{\text{int}}\sum_{i=1}^{N_{\text{int}}} S^i_{\alpha\alpha}$, where N_{int} is the number of internal atoms. As can be seen, for all types of nanowires, the average internal axial stress is proportional to D^{-1} and becomes small for diameters greater than ~50 nm. Additionally, nanowires with higher surfaces stresses (e.g., the [100] oriented square nanowire and circular nanowire) tend to develop larger internal stress. Even with the same axial orientation, less energetically favored surfaces, e.g., the irregular surfaces of circular nanowires, can lead to relatively higher internal axial stress as compared to nanowires with relatively energetically favored surfaces (i.e., the square nanowire). All these trends are consistent with Equation (1). The distribution of the atomic stress tensor component $S^i_{\alpha\alpha}$ (the insets in Fig. 1) shows that while the overall axial stress is zero, surface and interior atoms are subjected to very high opposite stresses (tensile and compressive stress for surface and interior atoms, respectively, in the current case). Additionally, the morphology of nanowire can lead to dramatic stress concentrations such as those around the corners of the square nanowire. The [110] oriented rhombic nanowire displays lower $S^i_{\alpha\alpha}$ for both surface and interior atoms, which might be due to the closely packed more stable {111} side surfaces as compared to the {100} surfaces of the <100> oriented square nanowire or the irregular surfaces of the circular nanowire. These features suggest that it is insufficient to characterize local SDN by the sample-wide average axial stress; surface stress should be an important consideration when dealing with SDN.

3.2. Sample-size-dependent activation enthalpy of SDN

Our direct calculations based on the modified ARTn method demonstrate that sample size indeed has significant effect on the activation barriers of SDN for sub-50 nm nanowires. Our samples are subjected to constant strains, which naturally leads to the activation Helmholtz free energy $\Delta F(\gamma,T)$, however, the activation Gibbs free energy can be obtained by setting $\Delta G(\sigma,T)$ to $\Delta F(\gamma,T)$, as

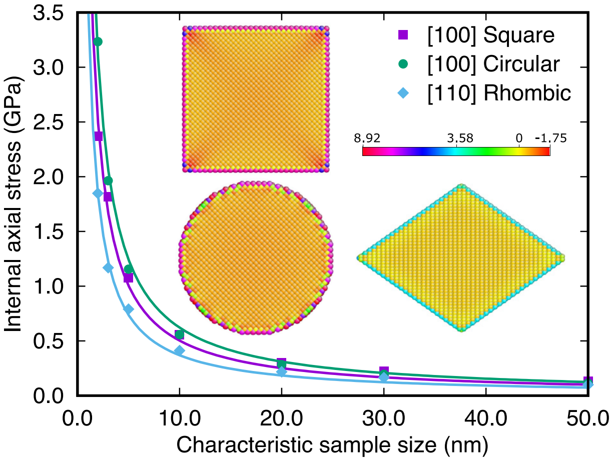

Fig. 1. The average internal axial stress and atomic axial stress distributions for free-standing nanowires of different geometry. Points are calculated data and curves are the best fit according to equation (1). The insets show atomic axial stress distributions of three typical nanowires with the characteristic size of 10 nm. Surface atoms are subject to tensile (positive) axial stress while the interior atoms are subject to compressive (negative) axial stress. Color bar indicates the range of atomic stress tensor component $S^i_{\alpha\alpha}$, in units of GPa. (For interpretation of the references to colour in this figure legend, the reader is referred to the web version of this article.)

long as σ corresponds to γ on the stress-strain curve for the perfect sample [43]. Also, the zero-*T* $\Delta G_0(\sigma)$ corresponds to the zero-*T* activation enthalpy $\Delta H(\sigma)$. Fig. 2 shows the activation enthalpy $\Delta H(\sigma_{app})$ of SDN, where σ_{app} is the applied axial stress. σ_{app} is calculated according to $\sigma_{app} = 1/N\sum_{i=1}^{N} S^i_{\alpha\alpha}$, where N is the total atom number, $S^i_{\alpha\alpha}$ is the axial component of the atomic stress tensor which is normalized by the average atomic volume of interior atoms (by averaging the atomic volumes obtained from Voronoi tessellation over the interior atoms). Typical saddle configurations for both the [100] nanowires and [110] nanowires are also shown as the insets of Fig. 2. For the [110] oriented rhombic nanowires, we found that the acute corners generally have lower ΔH than the obtuse corners for the same σ_{app} (see Fig. S1 in *Supplementary Materials* for details). As can be seen, $\Delta H(\sigma_{app})$ for both types of nanowires strongly depends on the nanowire sizes. For [100] oriented square nanowires under compression (Fig. 2a), ΔH becomes smaller with decreasing sample size D at a given σ_{app}. However, for [110] oriented rhombic nanowires under tension (Fig. 2b), an opposite trend is observed, i.e., ΔH becomes higher with decreasing sample sizes at a given σ_{app}. This opposite effect can be attributed to the surface-stress-induced internal *compressive* axial stress, which strengthens the nanowire under tensile load but weakens it under compressive load. To further demonstrate such loading mode effects, Fig. 2c and Fig. 2d show two more examples of [100] square nanowires under tension and [110] rhombic nanowires under compression. As can be seen, for [100] square nanowires under tension (Fig. 2c), ΔH now increases with decreasing sample size D. For [110] rhombic nanowires under compression (Fig. 2d), ΔH now decreases with decreasing sample size D. Both trends are reversed as the loading signs are flipped. This indicates that the opposite trend of ΔH vs. D is due to loading mode, rather than the nanowire geometry. Despite this reverse trend of $\Delta H(\sigma_{app})$ with respect to sample size D under different loading modes, both types of nanowires show diminishing size effect on $\Delta H(\sigma_{app})$ as σ_{app} approaches the athermal stress limit σ_{ath}. Similarly, relatively weak size effects were observed when the applied axial stress is relatively high, e.g., [100] nanowires under tension (Fig. 2c) and [110] nanowires under compression (Fig. 2d) show much higher σ_{app} (the leading partial has a smaller Schmid factor compared to that in Fig. 2a and Fig. 2b, thus leading to higher σ_{app}) than their counterparts in Fig. 2a and Fig. 2b but relatively weak size effects on ΔH. We will discuss how σ_{app} influences the size effects on ΔH later. Additionally, if we compare Fig. 2a and Fig. 2b where similar Schmid factor holds and relatively strong size effects show up, the [110] oriented rhombic nanowires overall display weaker sample size effects on $\Delta H(\sigma_{app})$ than that for the [100] oriented square nanowires, indicating the effect of the magnitude of surface stresses. In the following, we will use [100] square nanowires under compression and [110] rhombic nanowires under tension to demonstrate corresponding sample size effects.

Similar sample size effects on the activation volume (as defined by $\Omega_0 \equiv -\partial \Delta H / \partial \sigma_{app}$) are shown in Fig. 3. As can be seen, the overall magnitude of Ω_0 for SDN is $10^1\ b^3 - 10^2\ b^3$ (b is the magnitude of Burgers vector), consistent with previous studies. However, at a given axial stress, Ω_0 of different sized nanowires can differ by a significant factor, indicating strong sample size effects on the SDN process. Furthermore, the trend of Ω_0 vs. sample size at a given axial stress strongly depends on the sign of the axial stress. For example, for [100] square nanowires under compression, Ω_0 increases with increasing sample size; however, for [110] rhombic nanowires under tensile load, Ω_0 decreases with increasing sample size. We note that the 2 nm [110] rhombic nanowire shows smaller

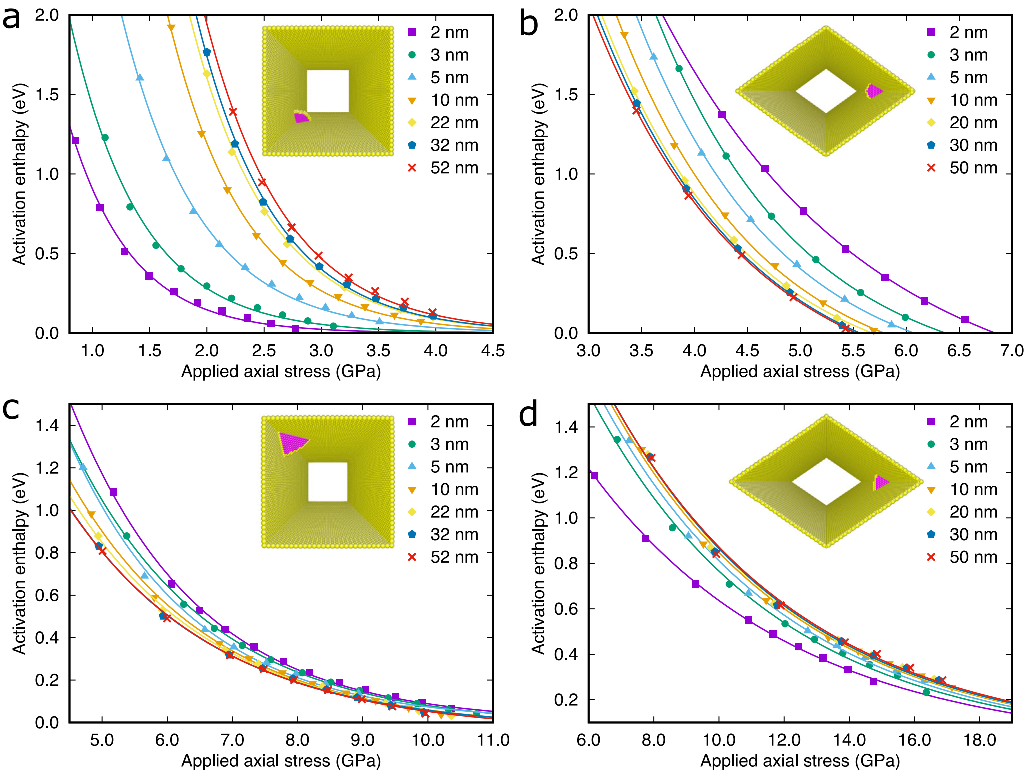

Fig. 2. Sample-size-dependent activation enthalpy $\Delta H(\sigma_{app})$ of SDN. (a) $\Delta H(\sigma_{app})$ for [100] oriented square nanowires under *compressive* loading. (b) $\Delta H(\sigma_{app})$ for [110] oriented rhombic nanowires under *tensile* loading. (c) $\Delta H(\sigma_{app})$ for [100] oriented square nanowires under *tensile* loading. (d) $\Delta H(\sigma_{app})$ for [110] oriented rhombic nanowires under *compressive* loading. Curves are fitting results to the calculated data (points), according to $\Delta H(\sigma_{app}) = A\{1 - \exp[\alpha(1 - \sigma_{app}/\sigma_{ath})]\}$[9], where A, α and σ_{ath} are fitting parameters. The insets show the nanowire shapes and typical saddle configurations of SDN. For convenience, both compressive and tensile stresses in are plotted as positive values.

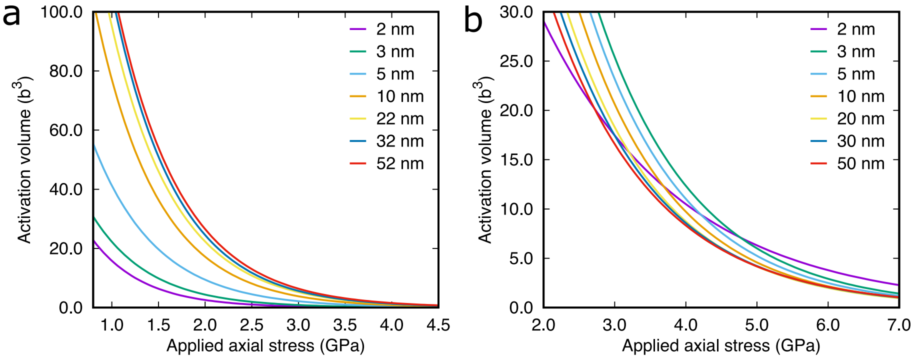

Fig. 3. Sample-size-dependent activation volume defined as $\Omega_0 \equiv -\partial\Delta H/\partial\sigma_{\mathrm{app}}$ of SDN. (a) Ω_0 for [100] oriented square nanowires under *compressive* loading. (b) Ω_0 for [110] oriented rhombic nanowires under *tensile* loading.

activation volume in the lower stress range compared to other sized nanowires, which might be due to the limited deformation volume of the sample. The above results clearly demonstrate that both surface stresses and the applied stress level have strong effects on the activation enthalpy ΔH and activation volume Ω_0 of SDN.

3.3. Effects of surface stresses on the activation enthalpy of SDN

The observed sample size effects on $\Delta H(\sigma_{\mathrm{app}})$ can be rationalized in terms of surface stresses as follows. When a nanowire is subjected to an external axial loading σ_{app}, the internal resolved shear stress distributes as $\tau(\mathbf{r}) = s\sigma_{\mathrm{app}} + \mathbf{b}\cdot\mathbf{S}_0(\mathbf{r})\cdot\mathbf{n}/|\mathbf{b}|$, where $\mathbf{r}$ is the atomic position vector, s is the Schmid factor, $\mathbf{b}$ is the Burgers vector, $\mathbf{n}$ is the unit normal vector of the slip plane and $\mathbf{S}_0(\mathbf{r})$ is the pre-existing atomic stress tensor induced by surface stress. For SDN, the local (a fixed position away from the corner) resolved shear stress can be further specified by a Taylor expansion in $1/D$.

$$\tau_{\mathrm{local}} = s\sigma_{\mathrm{app}} + \tau_0 + \tau_1\frac{1}{D} + O\left({}^{1}\!\big/_{D^2}\right) \tag{2}$$

where τ_0 and τ_1 are local constants depending on local geometry and surface stress. As can be seen, for a given σ_{app}, τ_{local} will additionally depend on the *sample size* (D) and *surface conditions* (τ_1). This leads to the sample dependence of SDN in terms of the activation enthalpy ΔH, assuming that ΔH is uniquely correlated with τ_{local}.

Our atomistic calculations show that the activation enthalpy ΔH is indeed uniquely correlated with the local resolved shear stress. Here the local resolved shear stress is identified as the local maximum resolved shear stress (LMRSS) τ_{lmrss}. This is because atoms with τ_{lmrss} are most likely to be involved in an emerging SDN event. The LMRSS is found by first calculating the atomic resolved shear stress$\tau^i = \mathbf{b}\cdot\mathbf{S}^i\cdot\mathbf{n}/|\mathbf{b}|$, where $\mathbf{S}^i$ is the full atomic stress tensor (taking into account both surface stress and the applied axial stress) for an interior atom *i*. **b, n,** $\mathbf{S}^i$ are all taken from the stressed but dislocation-free crystal (see Tables S1–S14 in *Supplementary Materials* for details). $\mathbf{S}^i$ is normalized by the atomic volume Ω_{i} from Voronoi tessellation. See the left panel in Fig. 4a for an example of the atomic resolved shear stress distribution in a dislocation-free [100] square nanowire. Then the LMRSS is identified by ranking τ^i for each interior atom that will be encompassed in the saddle dislocation loop of a SDN event (see the right panel in Fig. 4a for a typical saddle dislocation loop in a [100] oriented square nanowire), excluding surface atoms. Here the saddle dislocation loop configuration is identified by the common neighbor analysis [44,45]. In Fig. 4b, ΔH are plotted against τ_{lmrss} for all nanowires. As can be seen, all the data points that previously lie on different curves in Fig. 2 now collapse onto a single curve, for the [100] oriented square nanowire and the [110] oriented rhombic nanowire, respectively. This confirms that ΔH is indeed uniquely determined by τ_{lmrss}.

Fig. 5 shows the relation between τ_{lmrss} and σ_{app} for [100] oriented square nanowires (Fig. 5a) and [110] oriented rhombic nanowires (Fig. 5b). As can be seen, the LMRSS linearly depends on the applied axial stresses for a nanowire of a given size. The overall slopes of the linear relations from the best fitting in Fig. 5a and Fig. 5b are 0.46 and 0.44, which are slightly *smaller* than the non-deformed Schmid factors (0.47) for the leading partial dislocations, due to rotated **b**, **n** and deformed local atomic volume. Furthermore, different sized nanowires display different intercepts on the τ_{lmrss} axis, which indicates the effects of intrinsic surface stresses when $\sigma_{\mathrm{app}} = 0$ GPa. For the [100] oriented square nanowires under compressive loading, the absolute values of intercepts decrease with increasing sample sizes; however, the absolute values of intercepts increase with increasing sample sizes for the [110] oriented rhombic nanowires under tensile loading. This again confirms the weakening/strengthening effects for the compressive loading mode/tensile loading mode. Overall, the differences in intercepts for both kinds of nanowires become negligible when the sample size increases to approach 50 nm. The linear relations and sample size dependent intercepts shown in Fig. 5 have thus verified Equation (2) proposed above.

In Fig. 6, we decompose the activation enthalpy $\Delta H(\tau_{\mathrm{lmrss}})$ of SDN into several individual terms (such as ΔH_{core} due to dislocation core atoms, ΔH_{SF} due to stacking fault atoms, ΔH_{surf} due to surface ledge atoms and $\Delta H_{\mathrm{elastic}}$ due to elastic strains) to evaluate their relative contributions ($\Delta H(\tau_{\mathrm{lmrss}}) = \Delta H_{\mathrm{core}} + \Delta H_{\mathrm{SF}} + \Delta H_{\mathrm{surf}} + \Delta H_{\mathrm{elastic}}$). The individual contributing terms are calculated by comparing the energies of corresponding atoms in both the initial configurations and the saddle configurations. Atoms on stacking fault, dislocation core and surfaces are identified based on the common neighbor analysis [44,45]. In particular, atoms on saddle configuration surfaces with potential energy differing from the initial configuration by $|\Delta\mathrm{PE}| > 0.01$ eV are identified as surface ledge atoms. Fig. 6a shows the decomposed $\Delta H(\tau_{\mathrm{lmrss}})$ for [100] square nanowire. As can be seen, all individual contributions show excellent unique correlation with the LMRSS. Note that surface ledges created by SDN reduce the total potential energy in the case shown in Fig. 6a. This might be due to the corners of a [100] oriented square nanowire being not in truly Wulff shape equilibrium and the Burgers vector associated with the saddle dislocation loop (which displaces non-equilibrium surface atoms to relatively stable locations). Fig. 6b shows the potential energy differences between saddle configuration and the initial configuration for each surface atom. Surface ledges can be

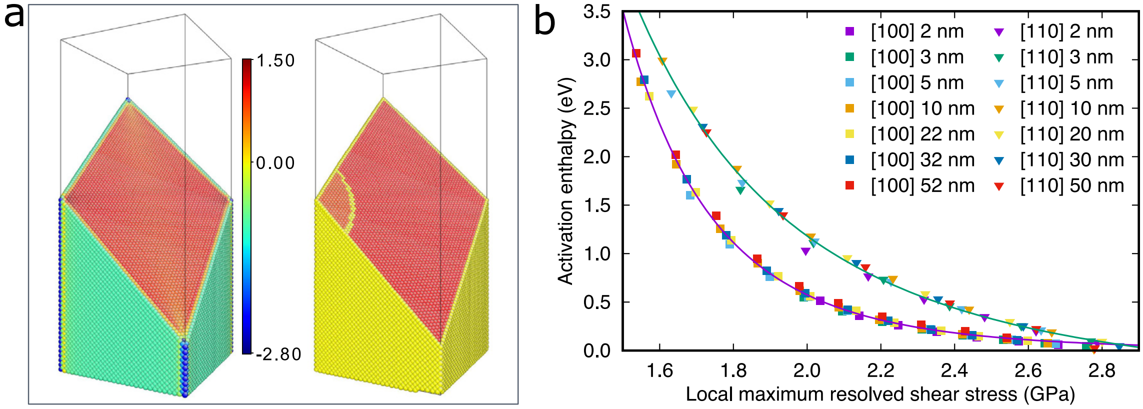

Fig. 4. Activation enthalpy of SDN is uniquely correlated with the local maximum resolved shear stress. (a) Atomic resolved shear stress distribution (the left panel) and typical saddle configuration of SDN in a [100] square nanowire (the right panel). Nanowires are cut along (111) plane. Color bar indicates the range of atomic resolved shear stress τ^i, in units of GPa. Defects are identified by common neighbor analysis. Yellow atoms represent surface atoms or dislocation core atoms; light red atoms represent stacking fault and red atoms are perfect face centered cubic atoms. (b) ΔH plotted against the local maximum resolved shear stress. Data points are calculated values and curves are fitted according the equation used in Fig. 2. (For interpretation of the references to colour in this figure legend, the reader is referred to the web version of this article.)

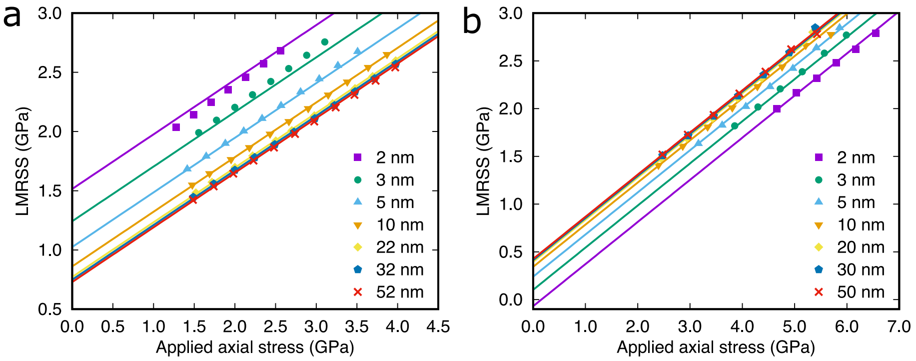

Fig. 5. Linear relationship between the LMRSS and applied axial stress for (a) [100] oriented square nanowires under compressive loading and (b) [110] oriented rhombic nanowires under tensile loading. Data points are fitted according to $\tau_{\mathrm{LMRSS}} = \alpha/D + \beta\sigma_{\mathrm{app}} + \tau_0$, where α, β and τ_0 are fitting parameters. For (a), $\alpha = 1.63$ J/m^2, $\beta = 0.46$, $\tau_0 = 0.70$ GPa. For (b), $\alpha = -1.03$ J/m^2, $\beta = 0.44$, $\tau_0 = 0.45$ GPa. For convenience, tensile stresses in (b) and corresponding LMRSS are plotted as positive values.

clearly seen due to sharp potential energy changes; the $|\Delta \mathrm{PE}|$ threshold chosen here largely captures the actual ledge length identified by the dislocation ends on surfaces. Similar $\Delta H(\tau_{\mathrm{lmrss}})$ decomposition and surface ledges identification by $|\Delta \mathrm{PE}|$ for [110] rhombic nanowire are shown in Fig. 6c and Fig. 6d. As can be seen, all individual contributions are again uniquely correlated with the LMRSS. However, the surface ledge contribution ΔH_{surf} is positive and the elastic strain contribution $\Delta H_{\mathrm{elastic}}$ is negative in this case. Generally, the sign of ΔH_{surf} should be closely related to surface condition and the Burgers vector of the nucleated dislocation. For [110] rhombic nanowire, the {111} side surfaces can be considered as stable surfaces such that most local perturbations, e.g., displacement field associated with the saddle dislocation loop, increase the potential energy. The elastic strain contribution $\Delta H_{\mathrm{elastic}}$ may simultaneously depend on the elastic field of nucleated dislocation, stacking fault, surface ledges and the work done by the applied stress. Together, they determine the sign of the overall elastic strain contribution $\Delta H_{\mathrm{elastic}}$. Despite these differences in $\Delta H(\tau_{\mathrm{lmrss}})$ decomposition for [100] square nanowires and [110] rhombic nanowires, the dislocation core contribution ΔH_{core} and surface ledge contribution ΔH_{surf} are significant in both cases, while stacking fault contribution ΔH_{SF} may be significant at relatively low LMRSS. Note that the enthalpy contribution ΔH_{SF} discussed here is not equivalent to the usually used stacking fault energy, as only energy changes of the *stacking fault atoms* (surrounding atoms of stacking fault are not taken into account) are considered. However, one can easily link ΔH_{SF} to the usually used stacking fault energy by a partition coefficient that distinguishes the contribution by stacking fault atoms and surrounding atoms, which can be accomplished using simple MD simulations. Similar analyses can also be applied to surface ledge atoms. These features further confirm the local nature of SDN and rationalize the unique correlation between ΔH and LMRSS.

The externally applied axial stress also plays an important role in the sample size dependence of ΔH for SDN. As discussed above, ΔH is uniquely correlated with τ_{lmrss} which however has a sample size dependent intercept in the linear relationship with σ_{app}, resulting in an apparent sample size dependence in terms of $\Delta H(\sigma_{\mathrm{app}}, D)$. However, when σ_{app} is sufficiently high such that the sample size dependent intercept (surface stress induced resolved shear stress $\tau_{\mathrm{surf}} \approx \tau_0 + \tau_1/D$) becomes inconsequential, ΔH will be dominated by σ_{app}, leading to a weak or even negligible sample size dependence of ΔH. This explains why the ΔH curves of different sized nanowires in Fig. 2 tend to merge together when σ_{app} approaches the athermal limit and those “hard orientations” deformed in Fig. 2c and Fig. 2d show relatively weak size effects. The size effects discussed here are the convoluted results of the loading conditions, surface conditions and the nature of bonding. For example, the yielding stress or σ_{app} at the elastic limit may depend on strain rates while the surface-induced resolved shear

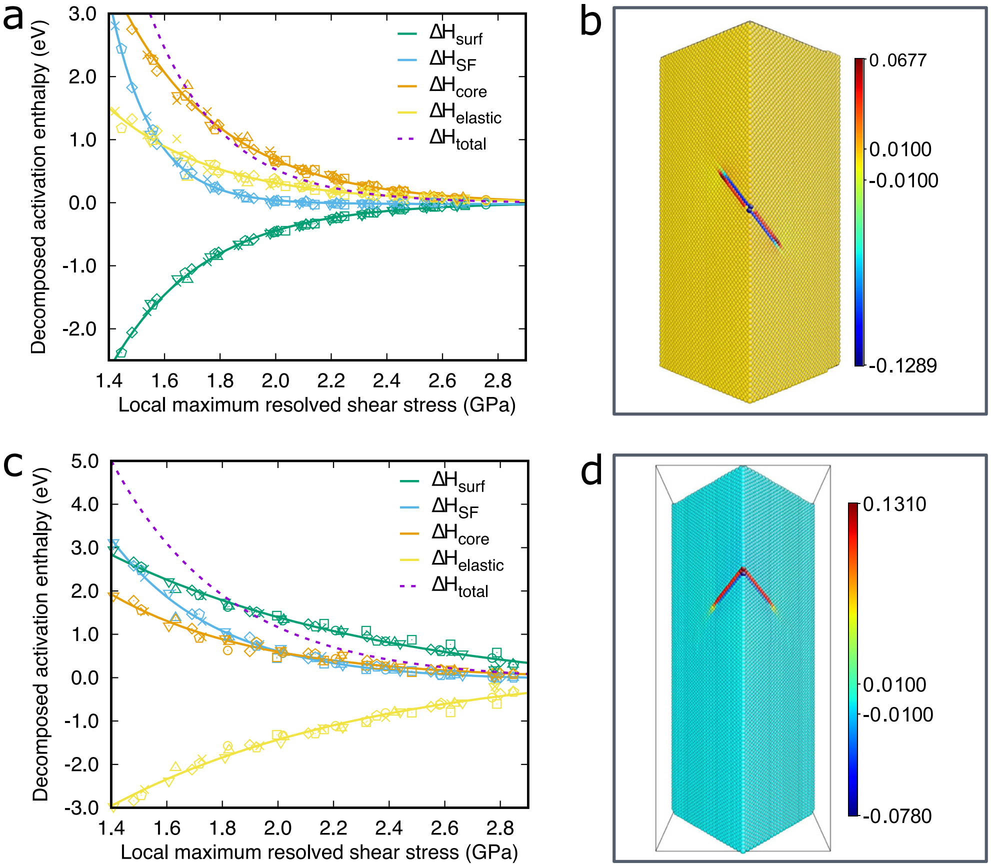

Fig. 6. Decomposition of activation enthalpy. (a) Decomposed activation enthalpy for [100] oriented square nanowires under compressive loading. (b) Potential energy difference between saddle configuration and initial configuration for each surface atom in a typical [100] square nanowire. (c) Decomposed activation enthalpy for [110] oriented rhombic nanowires under tensile loading. (d) Potential energy difference between saddle configuration and initial configuration for each surface atom in a typical [110] rhombic nanowire. Different marker shapes are used to represent different nanowire sizes. Data points are calculated values while curves are fits according to the equation used in Fig. 2. Color bars in (b) and (d) indicate the range of atomic potential energy difference, in units of eV. (For interpretation of the references to colour in this figure legend, the reader is referred to the web version of this article.)

stress τ_{surf} generally is insensitive to strain rates. As a result, $s\sigma_{app}$ may significantly increase and become dominant over τ_{surf} under high strain rates, leading to weak size effects in high-strain-rate deformations. In addition, the magnitude of σ_{app} at the elastic limit also strongly depends on the nature of bonding in materials. For example, if a material is intrinsically 'soft' (relatively weak bonding strength), the yielding stress or $s\sigma_{app}$ even under high-strain-rate deformation (such as MD simulations) may not dominate over τ_{surf} (surfaces can be quite energetically unfavored for irregular surfaces such as those of a circular nanowire), thus relatively strong size effects may still be observed. In contrast, a 'hard' material (strong bond) may show very high yielding stress regardless of the strain rates imposed such that $s\sigma_{app}$ completely overwhelms τ_{surf} even under low strain rates, resulting in weak or negligible size effects even with laboratory experiment strain rates.

3.4. Activation free energies at finite temperature

While low-temperature activation is dominated by the activation enthalpy, as temperature rises the activation entropy term $\Delta S(\sigma_{app}, D)$ has to be taken into account as they have been shown to significantly affect dislocation nucleation rate [32,46]. Our calculations show that $\Delta H(\sigma_{app})$ is insensitive to temperature for $T \leq 300$ K (see Fig. S2 in *Supplementary Materials*), which is consistent with previous studies [32,43]. Thus, the activation free energies at finite temperatures can be approximated as:

$$\Delta G(\sigma_{app}, T, D) \approx \Delta H(\sigma_{app}, D) - T\Delta S(\sigma_{app}, D) + O\left(T^2\right). \qquad (3)$$

In harmonic transition state theory, $\Delta S(\sigma_{app}, D)$ corresponds to the vibrational entropy difference between the PEL dividing surface astride the saddle point, and the ground state, sans the MEP direction [14]. $\Delta S(\sigma_{app}, D)$ tends to be positive because the "mountain pass" region tends to be vibrationally softer than the ground state. In Equation (3), we explicitly incorporate the sample size D dependence which has rarely been considered in previous studies probably due to expensive computational cost in evaluating the activation parameters for larger samples. Here we overcome this difficulty by a) directly obtaining $\Delta H(\sigma_{app}, D)$ for sub-50 nm samples based on the efficient specialized ARTn method; and b) validating the M-N compensation rule [38] ($\Delta S \approx \Delta H/T_{MN}$, where T_{MN} is a characteristic temperature) in the activation Gibbs free energy range of interest.

We have already shown the sample size dependent $\Delta H(\sigma_{app}, D)$, now let us validate the M-N rule. First we use thermodynamic integration method based on constrained molecular dynamics to calculate the activation Gibbs free energies $\Delta G(\sigma_{app}, T)$ at 300 K for 5 nm and 10 nm samples, respectively. The thermodynamic integration method is validated by comparing the SDN rate from direct MD simulations and the SDN rate predicted based on the ΔG obtained from thermodynamic integration method. For example, using the 5-nm square nanowire, we carried out 50 iso-configuration (with the same initial configuration but different atomic velocities) MD simulations under constant strain (the applied axial stress is ~2.05 GPa) at 300 K and obtained an average SDN rate of 3.5×10^8 s^{-1}. Meanwhile, the ΔG calculated from our thermodynamic integration method is 0.361 eV for the same sample. By using an attempt frequency in the range of [10^{11} s^{-1}, 10^{13} s^{-1}] and a total number of nucleation site 288 for this 5-nm square nanowire, we can predict the SDN rate to be in the range of [2.5×10^7 s^{-1}, 2.5×10^9 s^{-1}], which is consistent with the SDN rate from direct MD simulation, thus validating our thermodynamic integration method. After obtaining the activation Gibbs free energy at 300 K, the activation entropy is obtained by $\Delta S(\sigma_{app}) = (\Delta H(\sigma_{app}) - \Delta G(\sigma_{app},T))/T$. Fig. 7 shows the 300 K activation Gibbs free energy and the zero-T activation enthalpy as functions of σ_{app} for both types of nanowires. As can be seen, $\Delta G(\sigma_{app})$ at 300 K generally is much lower than the zero-T $\Delta H(\sigma_{app})$ at a given stress, manifesting significant entropic effects. Here, $\Delta G(\sigma_{app})$ in the range of [0.7 eV, 0.9 eV], as indicated by the shaded σ_{app} ranges in Fig. 7, is of particular interest as it generally corresponds to typical laboratory test conditions such as 300 K and strain rate of 10^{-2} s^{-1}. Correspondingly, for this range of $\Delta G(\sigma_{app})$, the zero-T $\Delta H(\sigma_{app})$ is largely in the range of [1.0 eV, 1.4 eV].

In Fig. 8, we plot the calculated activation entropy based on the results in Fig. 7. First of all, the magnitude of the calculated activation entropy is on the order of 10^1 k_B which suggests significant entropic effect on the nucleation rate (i.e., dislocation nucleation rate can be increased by a factor from e^{10} to e^{20}). Second, the calculated activation entropy is also subjected to significant sample size effects. For example, the activation entropy of 10-nm square nanowire under compression (Fig. 8a) is at least two times that for the 5-nm square nanowire. Similar size effects can also be seen for the rhombic nanowires in Fig. 8b. Finally, the size effects on activation entropy also depend the loading sign. Similar to the zero-T activation enthalpy shown in Fig. 2, activation entropy in Fig. 8a and Fig. 8b show opposite size effects with respect to the sign of loading, i.e., while the activation entropy increases with increasing sample size under compression, it decreases with increasing sample size under tension. These again demonstrate significant influence of surface stress and sample size. Note that surface stress can be positive or negative, so the loading sign effect may be entirely reversed if negative surface stress is present (i.e., Laplace pressure becomes negative).

Now we are in the position to validate the M-N rule. In Fig. 9, we plot the calculated activation entropy vs. zero-T activation enthalpy in the range of [1.0 eV, 1.4 eV] (the corresponding $\Delta G(\sigma_{app})$ is in the range of [0.7 eV, 0.9 eV]). As can be seen, for both types of nanowires, the activation entropy $\Delta S(\sigma_{app})$ largely correlates with $\Delta H(\sigma_{app})$ in a linear fashion, well consistent with the empirical M-N compensation rule. Such a simple linear relation between the activation entropy and activation enthalpy was also validated experimentally for various activation processes. However, its physical origin is still not well explained. One possible microscopic interpretation has been proposed by Yelon et al. [47,48], i.e., the M-N rule may result from the requirement for combining multiple

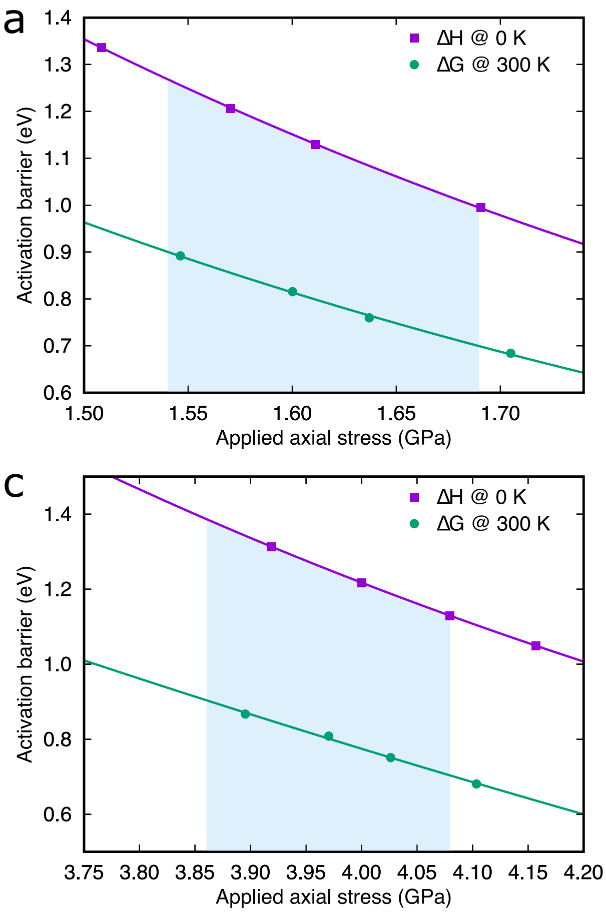

Fig. 7. The correspondence between zero-T activation enthalpy and activation Gibbs free energy at 300 K in the range relevant to laboratory experimental conditions. (a) 5 nm [100] square nanowire. (b) 10 nm [100] square nanowire. (c) 5 nm [110] rhombic nanowire. (d) 10 nm [110] rhombic nanowire. Shaded stress range corresponds to the activation Gibbs free energy range of [0.7 eV, 0.9 eV].

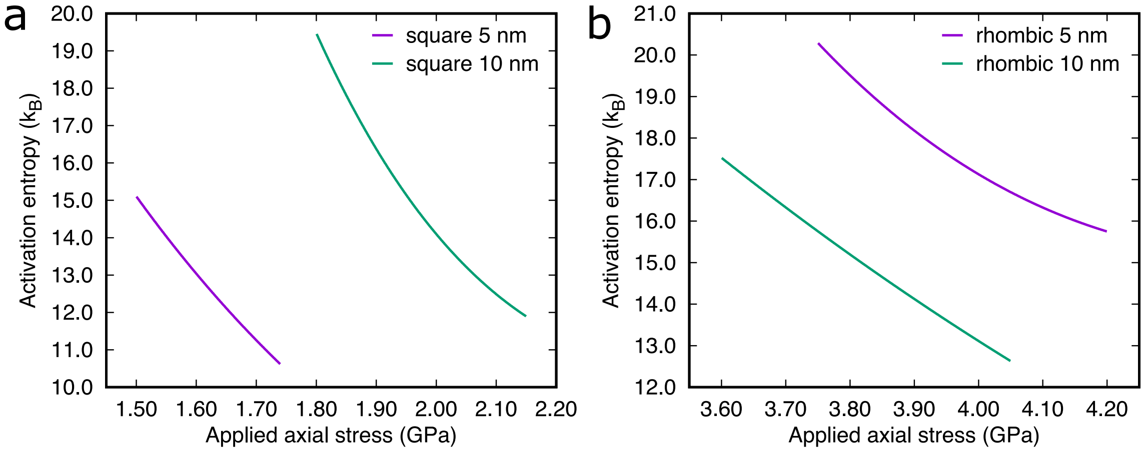

Fig. 8. Activation entropy for (a) [100] oriented square nanowires under compressive loading and (b) [110] oriented rhombic nanowires under tensile loading.

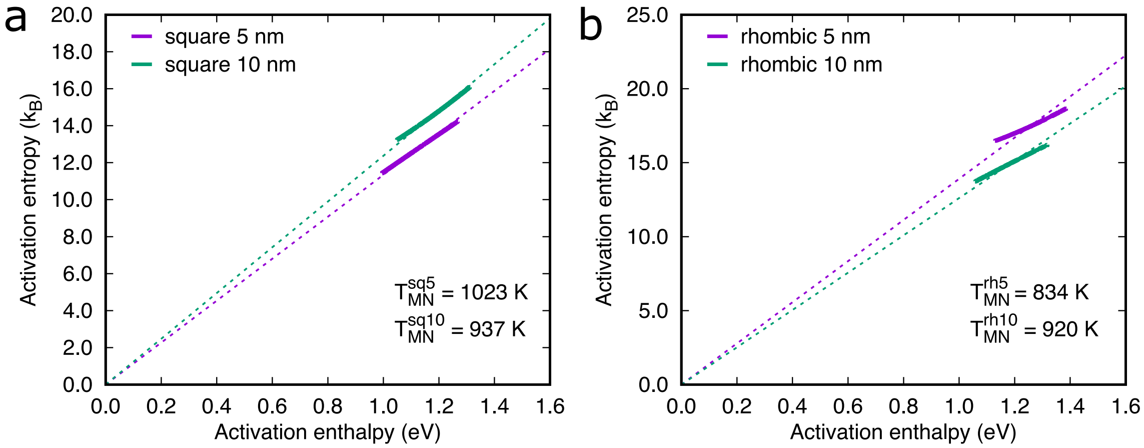

Fig. 9. Validation of the Meyer-Neldel compensation rule in the activation free energy range [0.7 eV, 0.9 eV]. (a) [100] oriented square nanowires under compressive loading. (b) [110] oriented rhombic nanowires under tensile loading. Solid lines are calculated values from the equation for $\Delta G(\sigma_{\mathrm{app}})$ and $\Delta H(\sigma_{\mathrm{app}})$ in Fig. 7, while dashed lines are linear fitting. The slopes of these linear fitting curves are denoted as $1/T_{\mathrm{MN}}$.

phonons inside the activation volume Ω (SDN can be recognized as a typical phonon-assisted process involving the stress-dependent activation volume Ω on the order of b^3-$10^1 b^3$). Specifically, as a process involves larger activation volume and enthalpy, more phonons are needed to overcome the barrier, causing larger entropy to be involved also in the activation process due to the increasing combinations (phases, amplitudes, modes) of phonons, e.g. acceptable fluctuations to the MEP that can still cause a transition.

Our numerical results demonstrated here show that the M-N rule largely holds for SDN in the activation Gibbs free energy range relevant to laboratory experiments where the activation barriers are relatively large. Due to expensive computational cost, we only focused on sub-10 nm samples; however, as can be seen in Fig. 9, even for 5 nm and 10 nm samples where significant surface stress effects are expected, the difference in T_{MN} is within ~100 K. This suggests a weak sample size dependence of T_{MN} in the activation Gibbs free energy range [0.7 eV, 0.9 eV]. So in the following, we will use the average T_{MN} calculated for 5 nm and 10 nm samples to estimate the activation free energies for other samples:

$$\Delta G(\sigma_{\mathrm{app}}, T, D) = \Delta H(\sigma_{\mathrm{app}}, D)\left(1 - \frac{T}{T_{\mathrm{MN}}}\right). \tag{4}$$

Note that the average T_{MN} obtained here is only valid for the activation Gibbs free energy range [0.7 eV, 0.9 eV] at 300 K, which generally corresponds to typical laboratory test conditions such as 300 K and strain rate of $10^{-2}\ \mathrm{s}^{-1}$. This enables an estimate of the nucleation stresses at experimentally relevant strain rates (seconds to hours).

3.5. Nucleation stress under typical laboratory conditions

Based on the calculated activation enthalpy and activation entropy above, we now estimate the most likely nucleation stresses for different sized nanowires, following the method used by Zhu et al. [8] The most likely nucleation stresses are obtained by numerically solving the following equation:

$$\frac{\Delta G(\sigma_{\mathrm{app}}, T, D)}{k_B T} = \ln \frac{k_B T N \upsilon_0}{E\dot{\varepsilon}\Omega(\sigma_{\mathrm{app}}, T, D)}, \tag{5}$$

where E is the Young's modulus, $\dot{\varepsilon}$ is strain rate, υ_0 is the attempt frequency and N is the number of equivalent nucleation sites. Here, we explicitly include the sample size dependence in both the activation Gibbs free energy and activation volume. Detailed values of the above parameters can be found in *Supplementary Materials*. Fig. 10 shows the nucleation stresses for both the [100] and [110] nanowires under laboratory experimental conditions ($T = 300$ K

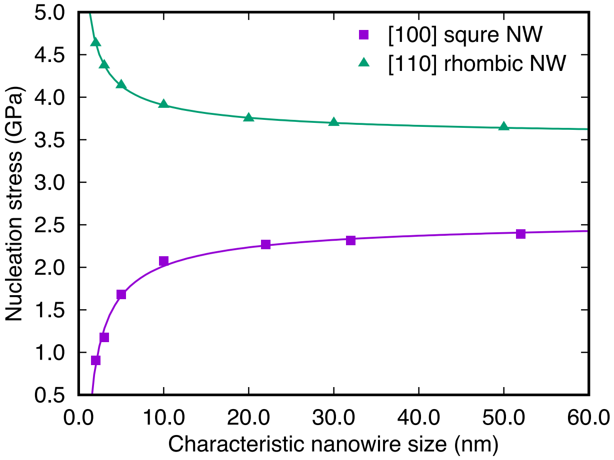

Fig. 10. Surface dislocation nucleation stress for [100] square nanowire (compressive loading) and [110] rhombic nanowire (tensile loading) under laboratory experiment conditions $T = 300$ K and $\dot{\varepsilon} = 10^{-2}\mathrm{s}^{-1}$.

and $\dot{\varepsilon} = 10^{-2}\mathrm{s}^{-1}$). As can be seen, the nucleation stress for [110] rhombic nanowires follows the widely believed “smaller is stronger” trend. In contrast, the nucleation stress of [100] square NWs rapidly decreases with decreasing sample sizes, resulting in a “smaller is weaker” trend. Such trends in axial strength with respect to nanowire size stem from the combined effects of surface stress and the applied stress. Since the SDN barriers are uniquely determined by the LMRSS which includes both contributions from surface stress ($\tau_{\mathrm{surf}} \approx \tau_0 + \tau_1/D$) and the applied axial stress ($s\sigma_{\mathrm{app}}$), i.e., LMRSS $= \tau_{\mathrm{surf}} + s\sigma_{\mathrm{app}}$, the minimum contribution from σ_{app} (i.e., the NW strength) to reach the LMRSS will directly depend on the magnitude and the sign of τ_{surf}. If τ_{surf} is opposite to $s\sigma_{\mathrm{app}}$, then it needs more σ_{app} for smaller samples to reach the LMRSS and hence “smaller is stronger”. However, if τ_{surf} has the same sign as $s\sigma_{\mathrm{app}}$, then it needs less σ_{app} for smaller samples to reach the LMRSS, thus “smaller is weaker”. It should be noted that this predicted strength-size trend may need to be modified in the very small size range where surface diffusion mediated process [49–51] could become significant [16,49] when the homologous temperature is sufficiently high.

4. Conclusions

In summary, based on a specialized activation-relaxation technique to directly calculate the activation barriers for expected events, we demonstrate that the zero-T activation enthalpy $\Delta H(\sigma_{\mathrm{app}})$ of surface dislocation nucleation strongly depends on sample sizes in the sub-50 nm regime. Despite the strong sample size dependence of $\Delta H(\sigma_{\mathrm{app}})$, we further find that ΔH is a unique function of the local maximum resolved shear stress τ_{lmrss} for a given nanowire shape, suggesting that τ_{lmrss} is a more intrinsic parameter that controls surface dislocation nucleation. Additionally, τ_{lmrss} shows linear relations with the applied stress with similar slope but different intercepts for different sized samples. These simple relations offer a shortcut to directly estimate $\Delta H(\sigma_{\mathrm{app}})$ for larger samples with more complex geometry based solely on the activation enthalpy calculated for a small sample, since τ_{lmrss} is a very local quantity. Individual energy terms, such as the core energy and surface ledge energy, are also found to collapse onto the single parameter family vs. τ_{lmrss}. Furthermore, thermodynamic integration method combined with constrained molecular dynamics was used to evaluate the activation free energies at finite temperatures. It turns out that the activation entropy has a significant effect on the dislocation nucleation rate and largely follows the Meyer-Neldel compensation rule in the activation Gibbs free energy range relevant to laboratory experiments. Finally, based on the activation enthalpy and activation entropy estimated from M-N rule, we found that, under typical laboratory experiment conditions, the most probable surface dislocation nucleation stress for different sized nanowires can either be “smaller is stronger” or “smaller is weaker”, depending on the combined effects of surface stress and applied stress. Our results may also have general relevance to many other nanostructured materials such as nanoparticles and nanocrystalline materials where surface or interface stress effects are significant.

Acknowledgement

This work was supported at JHU by US-DoE-BES-DMSE under Contract No. DE-FG02-16ER46056. Q.J.L. and E.M. acknowledge the computational resources from Maryland Advanced Research Computing Center (MARCC). S. H. acknowledges the MEXT-Supported Program for the Strategic Research Foundation at Private Universities, S1511002, 2015–2019. JL acknowledges support by NSF DMR-1410636.

Appendix A. Supplementary data

Supplementary data related to this article can be found at https://doi.org/10.1016/j.actamat.2017.11.048.

References

[1] G. Richter, K. Hillerich, D.S. Gianola, R. Mönig, O. Kraft, C.A. Volkert, Ultrahigh strength single crystalline nanowhiskers grown by physical vapor deposition, Nano Lett. 9 (2009) 3048–3052, https://doi.org/10.1021/nl9015107.

[2] J.-H. Seo, Y. Yoo, N.-Y. Park, S.-W. Yoon, H. Lee, S. Han, S.-W. Lee, T.-Y. Seong, S.-C. Lee, K.-B. Lee, P.-R. Cha, H.S. Park, B. Kim, J.-P. Ahn, Superplastic deformation of defect-free Au nanowires via coherent twin propagation, Nano Lett. 11 (2011) 3499–3502, https://doi.org/10.1021/nl2022306.

[3] L.Y. Chen, G. Richter, J.P. Sullivan, D.S. Gianola, Lattice anharmonicity in defect-free Pd nanowhiskers, Phys. Rev. Lett. 109 (2012) 125503. https://link.aps.org/doi/10.1103/PhysRevLett.109.125503.

[4] A. Sedlmayr, E. Bitzek, D.S. Gianola, G. Richter, R. Mönig, O. Kraft, Existence of two twinning-mediated plastic deformation modes in Au nanowhiskers, Acta Mater 60 (2012) 3985–3993. https://doi.org/10.1016/j.actamat.2012.03.018.

[5] J.-H. Seo, H.S. Park, Y. Yoo, T.-Y. Seong, J. Li, J.-P. Ahn, B. Kim, I.-S. Choi, Origin of size dependency in coherent-twin-propagation-mediated tensile deformation of noble metal nanowires, Nano Lett. 13 (2013) 5112–5116, https://doi.org/10.1021/nl402282n.

[6] B. Roos, B. Kapelle, G. Richter, C.A. Volkert, Surface dislocation nucleation controlled deformation of Au nanowires, Appl. Phys. Lett. 105 (2014) 201908, https://doi.org/10.1063/1.4902313.

[7] L.Y. Chen, M. He, J. Shin, G. Richter, D.S. Gianola, Measuring surface dislocation nucleation in defect-scarce nanostructures, Nat. Mater 14 (2015) 707–713, https://doi.org/10.1038/nmat4288.

[8] T. Zhu, J. Li, A. Samanta, A. Leach, K. Gall, Temperature and strain-rate dependence of surface dislocation nucleation, Phys. Rev. Lett. 100 (2008) 25502. https://link.aps.org/doi/10.1103/PhysRevLett.100.025502.

[9] C.R. Weinberger, A.T. Jennings, K. Kang, J.R. Greer, Atomistic simulations and continuum modeling of dislocation nucleation and strength in gold nanowires, J. Mech. Phys. Solids 60 (2012) 84–103. https://doi.org/10.1016/j.jmps.2011.09.010.

[10] A.T. Jennings, C.R. Weinberger, S.-W. Lee, Z.H. Aitken, L. Meza, J.R. Greer, Modeling dislocation nucleation strengths in pristine metallic nanowires under experimental conditions, Acta Mater 61 (2013) 2244–2259, https://doi.org/10.1016/j.actamat.2012.12.044.

[11] Y. Lu, J. Song, J.Y. Huang, J. Lou, Surface dislocation nucleation mediated deformation and ultrahigh strength in sub-10-nm gold nanowires, Nano Res. 4 (2011) 1261–1267, https://doi.org/10.1007/s12274-011-0177-y.

[12] H. Zheng, A. Cao, C.R. Weinberger, J.Y. Huang, K. Du, J. Wang, Y. Ma, Y. Xia, S.X. Mao, Discrete plasticity in sub-10-nm-sized gold crystals, Nat. Commun. 1 (2010) 144. https://doi.org/10.1038/ncomms1149.

[13] E. Rabkin, D.J. Srolovitz, Onset of plasticity in gold nanopillar compression, Nano Lett. 7 (2007) 101–107, https://doi.org/10.1021/nl0622350.

[14] J. Li, The mechanics and physics of defect nucleation, MRS Bull. 32 (2007) 151–159, https://doi.org/10.1557/mrs2007.48.

[15] A.T. Jennings, J. Li, J.R. Greer, Emergence of strain-rate sensitivity in Cu

nanopillars: transition from dislocation multiplication to dislocation nucleation, Acta Mater 59 (2011) 5627–5637. https://doi.org/10.1016/j.actamat.2011.05.038.

[16] J. Li, Dislocation nucleation: diffusive origins, Nat. Mater 14 (2015) 656–657. https://doi.org/10.1038/nmat4326.

[17] S. Hara, S. Izumi, S. Sakai, Reaction pathway analysis for dislocation nucleation from a Ni surface step, J. Appl. Phys. 106 (2009) 93507, https://doi.org/10.1063/1.3254178.

[18] S. Brochard, P. Hirel, L. Pizzagalli, J. Godet, Elastic limit for surface step dislocation nucleation in face-centered cubic metals: temperature and step height dependence, Acta Mater 58 (2010) 4182–4190. https://doi.org/10.1016/j.actamat.2010.04.009.

[19] Z.-J. Wang, Q.-J. Li, Y.-N. Cui, Z.-L. Liu, E. Ma, J. Li, J. Sun, Z. Zhuang, M. Dao, Z.-W. Shan, S. Suresh, Cyclic deformation leads to defect healing and strengthening of small-volume metal crystals, Proc. Natl. Acad. Sci. 112 (2015) 13502–13507, https://doi.org/10.1073/pnas.1518200112.

[20] F.G. Sen, A.T. Alpas, A.C.T. van Duin, Y. Qi, Oxidation-assisted ductility of aluminium nanowires, Nat. Commun. 5 (2014) 3959. https://doi.org/10.1038/ncomms4959.

[21] R.C. Cammarata, Surface and interface stress effects in thin films, Prog. Surf. Sci. 46 (1994) 1–38. https://doi.org/10.1016/0079-6816(94)90005-1.

[22] S. Izumi, S. Hara, T. Kumagai, S. Sakai, A method for calculating surface stress and surface elastic constants by molecular dynamics: application to the surface of crystal and amorphous silicon, Thin Solid Films 467 (2004) 253–260. https://doi.org/10.1016/j.tsf.2004.03.034.

[23] S. Hara, S. Izumi, T. Kumagai, S. Sakai, Surface energy, stress and structure of well-relaxed amorphous silicon: a combination approach of ab initio and classical molecular dynamics, Surf. Sci. 585 (2005) 17–24. https://doi.org/10.1016/j.susc.2005.03.061.

[24] V.B. Shenoy, Atomistic calculations of elastic properties of metallic fcc crystal surfaces, Phys. Rev. B 71 (2005) 94104. https://link.aps.org/doi/10.1103/PhysRevB.71.094104.

[25] T. Frolov, Y. Mishin, Temperature dependence of the surface free energy and surface stress: an atomistic calculation for Cu(110), Phys. Rev. B 79 (2009) 45430. https://link.aps.org/doi/10.1103/PhysRevB.79.045430.

[26] C.R. Weinberger, W. Cai, Plasticity of metal nanowires, J. Mater. Chem. 22 (2012) 3277–3292, https://doi.org/10.1039/C2JM13682A.

[27] J. Diao, K. Gall, M.L. Dunn, Yield strength asymmetry in metal nanowires, Nano Lett. 4 (2004) 1863–1867, https://doi.org/10.1021/nl0489992.

[28] W. Zhang, T. Wang, X. Chen, Effect of surface stress on the asymmetric yield strength of nanowires, J. Appl. Phys. 103 (2008) 123527, https://doi.org/10.1063/1.2946447.

[29] G.E. Beltz, L.B. Freund, On the nucleation of dislocations at a crystal surface, phys, Status Solidi 180 (1993) 303–313, https://doi.org/10.1002/pssb.2221800203.

[30] C.E. Carlton, L. Rabenberg, P.J. Ferreira, On the nucleation of partial dislocations in nanoparticles, Philos. Mag. Lett. (2008), https://doi.org/10.1080/09500830802307641.

[31] G. Xu, C. Zhang, Analysis of dislocation nucleation from a crystal surface based on the Peierls–Nabarro dislocation model, J. Mech. Phys. Solids 51 (2003) 1371–1394. https://doi.org/10.1016/S0022-5096(03)00067-X.

[32] S. Hara, J. Li, Adaptive strain-boost hyperdynamics simulations of stress-driven atomic processes, Phys. Rev. B 82 (2010) 184114. https://link.aps.org/doi/10.1103/PhysRevB.82.184114.

[33] T. Zhu, J. Li, A. Samanta, H.G. Kim, S. Suresh, Interfacial plasticity governs strain rate sensitivity and ductility in nanostructured metals, Proc. Natl. Acad. Sci. 104 (2007) 3031–3036, https://doi.org/10.1073/pnas.0611097104.

[34] K. Kang, Atomistic Modelling of Fracture Mechanisms in Semiconductor Nanowires under Tension, Stanford University, 2010.

[35] N. Mousseau, G.T. Barkema, Traveling through potential energy landscapes of disordered materials: the activation-relaxation technique, Phys. Rev. E 57 (1998) 2419–2424. https://link.aps.org/doi/10.1103/PhysRevE.57.2419.

[36] E. Cancès, F. Legoll, M.-C. Marinica, K. Minoukadeh, F. Willaime, Some improvements of the activation-relaxation technique method for finding transition pathways on potential energy surfaces, J. Chem. Phys. 130 (2009) 114711, https://doi.org/10.1063/1.3088532.

[37] N. Mousseau, L.K. Béland, P. Brommer, J.-F. Joly, F. El-Mellouhi, E. Machado-Charry, M.-C. Marinica, P. Pochet, The activation-relaxation technique: ART nouveau and kinetic ART, J. At. Mol. Opt. Phys. 2012 (2012) 925278. https://doi.org/10.1155/2012/925278.

[38] M. Meyer, H. Neldel, Relation between the energy constant and the quantity constant in the conductivity–temperature formula of oxide semiconductors, Z. Tech. Phys. 12 (1937) 588.

[39] Y. Mishin, M.J. Mehl, D.A. Papaconstantopoulos, A.F. Voter, J.D. Kress, Structural stability and lattice defects in copper: ab initio, tight-binding, and embedded-atom calculations, Phys. Rev. B 63 (2001) 224106. https://link.aps.org/doi/10.1103/PhysRevB.63.224106.

[40] G. Henkelman, B.P. Uberuaga, H. Jónsson, A climbing image nudged elastic band method for finding saddle points and minimum energy paths, J. Chem. Phys. 113 (2000) 9901–9904, https://doi.org/10.1063/1.1329672.

[41] S. Plimpton, Fast parallel algorithms for short-range molecular dynamics, J. Comput. Phys. 117 (1995) 1–19. https://doi.org/10.1006/jcph.1995.1039.

[42] J. Li, AtomEye: an efficient atomistic configuration viewer, Model. Simul. Mater. Sci. Eng. 11 (2003) 173. http://stacks.iop.org/0965-0393/11/i=2/a=305.

[43] S. Ryu, K. Kang, W. Cai, Predicting the dislocation nucleation rate as a function of temperature and stress, J. Mater. Res. 26 (2011) 2335–2354, https://doi.org/10.1557/jmr.2011.275.

[44] D. Faken, H. Jónsson, Systematic analysis of local atomic structure combined with 3D computer graphics, Comput. Mater. Sci. 2 (1994) 279–286. https://doi.org/10.1016/0927-0256(94)90109-0.

[45] H. Tsuzuki, P.S. Branicio, J.P. Rino, Structural characterization of deformed crystals by analysis of common atomic neighborhood, Comput. Phys. Commun. 177 (2007) 518–523. https://doi.org/10.1016/j.cpc.2007.05.018.

[46] S. Ryu, K. Kang, W. Cai, Entropic effect on the rate of dislocation nucleation, Proc. Natl. Acad. Sci. 108 (2011) 5174–5178, https://doi.org/10.1073/pnas.1017171108.

[47] A. Yelon, B. Movaghar, Microscopic explanation of the compensation (Meyer-Neldel) rule, Phys. Rev. Lett. 65 (1990) 618–620. https://link.aps.org/doi/10.1103/PhysRevLett.65.618.

[48] A. Yelon, B. Movaghar, R.S. Crandall, Multi-excitation entropy: its role in thermodynamics and kinetics, Rep. Prog. Phys. 69 (2006) 1145. http://stacks.iop.org/0034-4885/69/i=4/a=R04.

[49] L. Tian, J. Li, J. Sun, E. Ma, Z.-W. Shan, Visualizing size-dependent deformation mechanism transition in Sn, Sci. Rep. 3 (2013) 2113. https://doi.org/10.1038/srep02113.

[50] J. Sun, L. He, Y.-C. Lo, T. Xu, H. Bi, L. Sun, Z. Zhang, S.X. Mao, J. Li, Liquid-like pseudoelasticity of sub-10-nm crystalline silver particles, Nat. Mater 13 (2014) 1007–1012. https://doi.org/10.1038/nmat4105.

[51] L. Zhong, F. Sansoz, Y. He, C. Wang, Z. Zhang, S.X. Mao, Slip-activated surface creep with room-temperature super-elongation in metallic nanocrystals, Nat. Mater 16 (2017) 439–445. https://doi.org/10.1038/nmat4813.